A high-speed vertical transition for multi-layer AlN carrier boards designed by time-domain reflectometry

M. A. Jezzini[1], **P. J. Marraccini**[1,2], **and F. H. Peters**[1,3]

[1]Tyndall National Institute, Cork, Ireland
[2]Apple, California, USA
[3]University College Cork, Cork, Ireland

Abstract— High density, high speed photonic integrated circuits (PICs) have large numbers of closely spaced DC and RF contacts, which must be connected in the package. The use of multi-layer carrier boards to interface between the contacts and the package gives high performance and high density. In order to be effective as a packaging solution, these multi-layer carrier boards need high-speed electrical channels with good performance. Also, the boards usually need high thermal conductivity to manage the heat. Co-fired aluminium nitride (AlN) has the needed high thermal conductivity. However, there are no designs of multi-layer high-speed channels in the literature for co-fired AlN. Therefore, this article presents a high-speed multi-layer channel for co-fired AlN and its measured results. Two transmission lines were designed that showed a measured loss of $\approx 0.09\,\mathrm{dB\,mm^{-1}}$ at 40 GHz. The vertical transition allows for arbitrary planar rotations of the channel and showed a measured 3 dB bandwidth of 33 GHz and small penalties in the eye diagram with a $44\,\mathrm{Gbit\,s^{-1}}$ signal. The channels showed crosstalk below −30 dB.

1. INTRODUCTION

Photonic devices are evolving to photonic integrated circuits (PICs) with high circuit-density and high channel-speed [1]. These PICs need packaging solutions that accommodate the high circuit density and high-speeds. One of these packaging solutions is the use of multi-layer carrier boards that work as interposers with the package connectors. The use of these multi-layer carrier boards together with flip-chip can eliminate the need for a large number of wire-bonds, which add greatly to the overall expense and create problems with the high-speed signals. The concept of using multi-layer boards to integrate devices has been called system-on-package (SoP) [2] and it could help to meet the stringent size, cost, and performance requirements of today markets, which cannot be achieved by conventional single-layer carrier boards. The multi-layer carrier board in a photonic packaging must provide a good microwave performance and frequently a high thermal conductivity [3]. This contrast to high-speed wireless applications that have very small thermal requirements, and therefore use materials with the lowest microwave loss. From the materials that offer low microwave loss, the two most commonly used are low-temperature co-fired ceramic (LTCC) and liquid crystal polymers (LCP) [4]. One problem with both LTCC and LCP is their low thermal conductivity (Table 1). In contrast, aluminium nitride (AlN) has high thermal conductivity (Table 1 and [5]) and AlN is offered as a multi-layer high-temperature co-fired ceramics which make AlN an attractive material for making multi-layer carrier boards for PICs. However, there are not designs of multi-layer high-speed channels available in the literature for co-fired AlN.

A high-speed multi-layer channel for co-fired AlN and its measured results are presented in this work. We have designed, fabricated, and characterised a novel vertical transition between a conductor-backed co-planar waveguide (CB-CPW) and a shielded multi-layer co-planar waveguide (SM-CPW) that is rotatable (Fig. 1). This transition is an improvement of a transition in LTCC designed by the authors and published in [6] and now allows rotations at an arbitrary angle as shown in Fig. 2. The rotation capability is helpful for the routing and the crossing of channels in a high-density interposer.

2. DESIGN OF THE CHANNELS

The transition consists of three ceramic layers (Fig. 1). Layer D00 is 127 µm thick and layers D01 and D02 are 254 µm thick. The metal is gold with a thickness of 3 µm for all the layers. The names of the metal layers (name starts with C) and the vias layers (name starting with V) are defined in Fig. 1. The rest of the dimensions that define the transition are shown in Fig. 3 and given in Table 2.

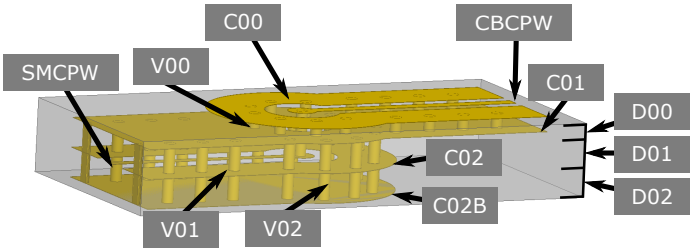

Figure 1: The vertical transition is between a CBCPW and a SMCPW

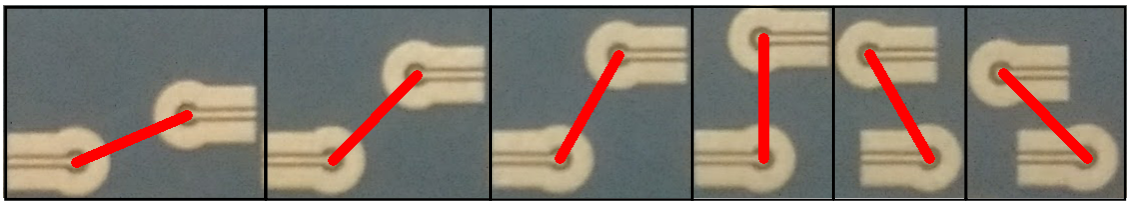

Figure 2: The transition allows rotation at an arbitrary angle

The manufacturing design rules force the minimum metal width to 100 µm, the spacing between vias (i) greater than 300 µm, and the via catch pad (h) greater than 75 µm. The co-planar ground width (g) is large enough to fit the ground vias and minimise the loss. The CB-CPW dimensions (s and a) and the SM-CPW dimensions (n and l) were defined by simulating the transmission line in ANSYS 2D Extractor to get 50 Ω characteristic impedance and the smaller dimensions that can be fabricated. The other dimensions (c, p, t, v and o) were defined by manually tuning them to minimize the reflection of a time domain reflectometry (TDR) model.

The TDR model is simulated using the full-wave time-domain electromagnetic solver (ANSYS HFSS), using the TDR results to locate the source of reflections and then manually modifying the parametric dimensions that form the vertical transitions to minimise the reflections. This is following a similar procedure to [8]. The reason for taking this approach is that the frequency-domain simulation results given by the S-parameters give us information of the performance of the overall transition but does not point to the location of the source of reflections. In contrast, the time-domain information can be mapped to a position of the source of the reflection and thus give us more information for the optimization. The full-wave model includes a top layer of air with a thickness of 500 µm. The material models used are given in Table 3.

A novel port was created for the full-wave time-domain electromagnetic solver (Fig. 5). The time-domain full-wave electromagnetic solver does not allow for wave-ports in the case of a CPW since the transmission line has multiple dielectrics and a lossy dielectric. A standard lumped port was created (Fig. 5a) based on the software documentation and on [9, 10, 11, 12, 13, 14]. The standard lumped port resulted produced a notable reflection (Fig. 5c). To reduce this reflection created by the port, a novel version (Fig. 5b) was created in this research which reduces the reflections from the port compared to the standard lumped port (Fig. 5c). The idea of the novel lumped port is to surround the three-leg standard lumped port by a box of perfectly conducting surfaces. The novel lumped port uses a standard three-leg lumped port but, in order to be able to surround it by a perfectly conducting surface, it is placed horizontally on top of the substrate surface where the co-planar metals lay. Surrounding boxes of air and AlN are added. A perfectly conducting surface condition is applied to the faces of this box except for the faces where the three-leg lumped port sits and the faces normal to the transmission line direction and touches the transmission line.

Table 1: AlN has much better thermal conductivity and equivalent RF performance [7][4].

	LTCC	LCP	AlN
Thermal conductivity	2.0 to 4.4	0.2	150
Dielectric constant	5.7 to 9.1	2.9 to 3.2	8.5
Tangent loss	0.0020	0.0025	0.0030

Table 2: Some dimensions in µm of the fabricated transition

s	a	g	c	p	i	t	h	v	l	n	o
120	120	500	450	200	$\gtrapprox$ 300	150	75	100	200	100	650

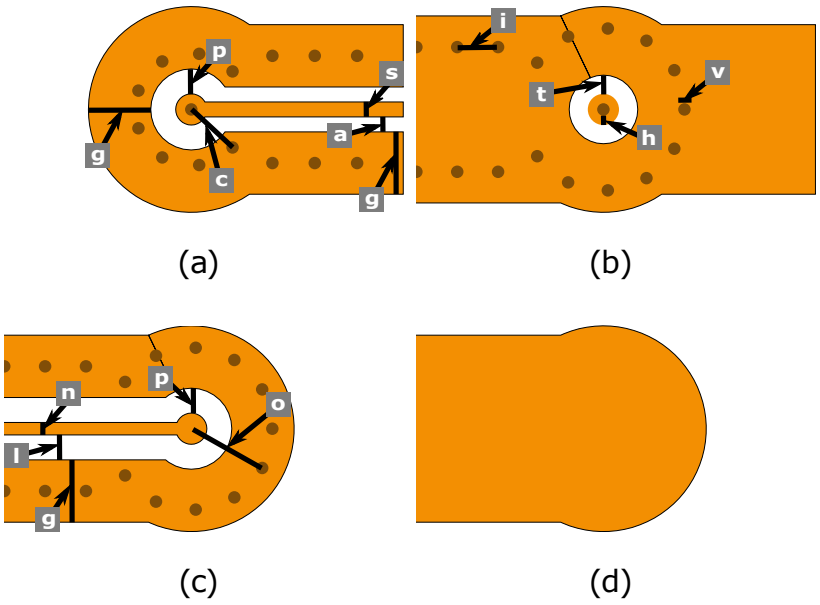

Figure 3: The dimensions that define the transition are given in Table 2. (a) C00 and V00. (b) C01 and V01. (c) C02 and V02. (d) C02B.

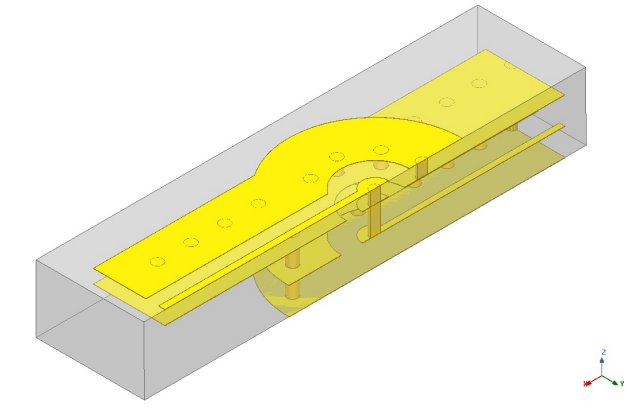

Figure 4: The geometry imported to the time-domain full-wave electromagnetic solver.

Table 3: The materials properties used for the electromagnetic simulations. The values for gold and air are the defaults in the software. LTCC based on the datasheet provided by supplier.

Material	ϵ_r	μ_r	σ [S m^{-1}]	tan δ
Gold	1.0	1	41×10^6	–
Air	1.0	1	–	0.000
AlN	8.2	1	–	0.001

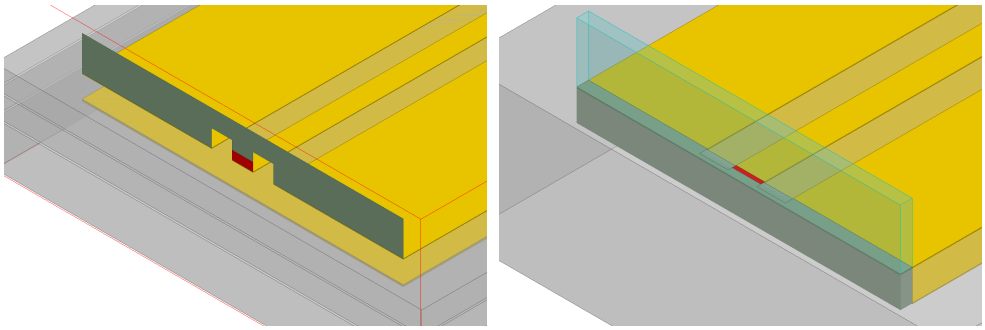

(a) Standard (b) Novel

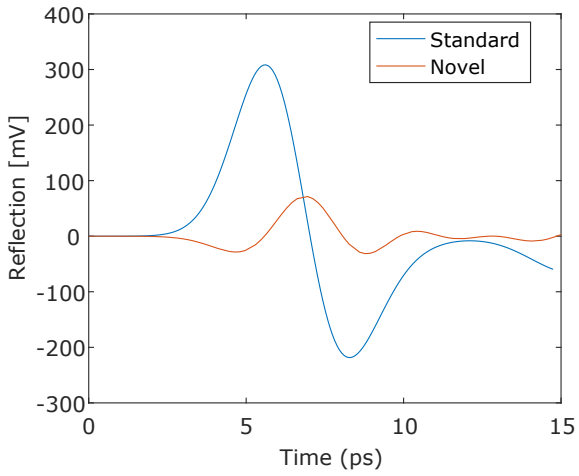

(c) Reflections

Figure 5: The lumped ports created for the time-domain full-wave electromagnetic solver. The novel version, created in this research, reduces the reflections from the port compared to the standard lumped port. The input amplitude is 1 V.

Two of the dimensions of these boxes are chosen to match with the two dimensions of the three-leg lumped port. The height of the air box must be large enough to avoid coupling from the small square port to the top surface of the air box. The height of the AlN box is chosen as the distance between the coplanar metals and the backside ground metal. In this way, the grounds at the two levels are shorted together by the perfectly conducting surface conditions at the faces of the box. Finally, the dimension of the lumped port in the direction of the transmission line must be small enough to avoid resonances at frequencies contained by the input voltage profile but as large as possible to avoid increasing the number of points in the mesh around the port. A port that is too small consumes a lot more computer memory and computational time. In our case, the port is 20 µm for a Gaussian input profile with a Full width at half maximum (FWHM) of 3 ps.

The solver was set up to use a Gaussian input profile with an FWHM of 3 ps (Fig. 6a). The shorter the pulse the more detail that the reflections can resolve. However, the shorter the pulse the finer the meshing and thus the higher the memory and computer time. The 3 ps pulse is the shortest that the memory in the available computer was able to simulate. The time step is set to 0.1655 ps. The profile shown in Fig. 6a is maintained as 0 V after 15 ps. The 3 ps pulse has a spectral content with frequencies up to 300 GHz (Fig. 6b). The model is surrounded by the outer boundary condition set to radiation.

The results can be used to identify the regions that are creating the unwanted reflections. For example, the simulated reflection for the initial version of the AlN transition using the same design procedure as in [6] is presented in Fig. 7a. The reflection has the highest reflection at time 33 ps. This is the reflection measured at the port, therefore, the event that created this reflection occurred at half this time (i.e. 16.5 ps). This is because the reflected signal has to travel back to the port and it takes exactly the same time for the pulse to get to the source of the reflection as it does to come back to the port. Once the timing of the event has been located, the fields can be inspected

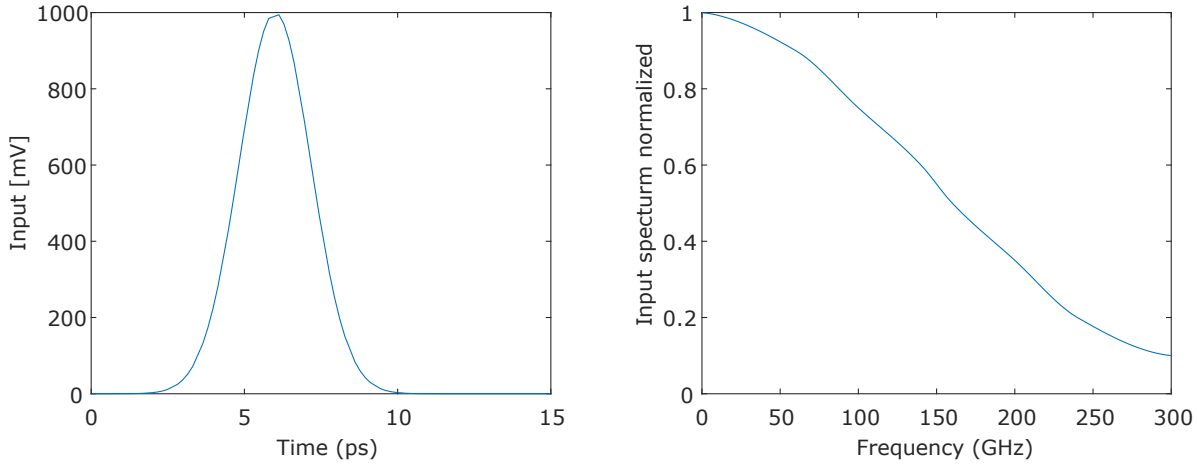

Figure 6: The input voltage profile used in the time-domain simulations.

to translate this reflection to a location in the geometry of the transition. For example, Fig. 7b shows the field at the cross-section at the centre of the transition at the closest time of the event that was solved by the simulator (16.6 ps). One question that remains is how much the reflected voltage is affected by the input voltage profile and the multiple reflections the pulse creates before coming back to the port.

A novel impedance profile reconstruction algorithm has been created. The algorithm is a generalization of the algorithm in [15, 16] to work with arbitrary inputs instead of only step inputs. The algorithm is used to recover an impedance profile that takes into account the shape of the input voltage waveform and the multiple reflections that occur in the transition. The reconstruction fails when using the Gaussian input profile. The algorithm presents non-linear oscillations that the stabilisation modification is not able to solve for the impedance profile. Based on the full-wave electromagnetic solver documentation, the input voltage profile and the reflection are integrated. After integration, the input profile is similar to the Heaviside's step function (Fig. 8a). The reflected voltage is also integrated (Fig. 8b). The integrated input voltage and integrated reflected voltage are used in the impedance reconstruction by a TDR algorithm. The input voltage starts at zero and thus the algorithm presents problems with division by zero and numerical errors. Therefore, the first 5 ps of the input voltage and the reflected voltage were removed, setting the front-wave voltage to 500 mV. The resulting impedance profile (Fig. 8c) takes into account the shape of the input profile and the multiple reflections in the device.

The vertical transition was manually optimised by using the time-domain full-wave simulation and the impedance recovery algorithm. The optimisation process consisted of performing the time-domain full-wave simulation, using the results in the impedance reconstruction algorithm by TDR, locating the regions that generate the maximum impedance mismatch and then manually changing design parameters related to the localised region. A total of 36 different versions were simulated. The variable that made a larger change in the simulated results is the radius of the coaxial iris in the CB-CPW backside ground metal (`t`). A optimization sweep in `t` showed that the design works better if `t` is smaller than the gap in the coaxial-like catch pads (`p`) which allows for rotations of the design. The comparison between the starting design and the final design is shown in Fig. 9a. The impedance profile of the final version shows a low characteristic impedance section centred at 42 ps. This feature can't be removed by changing any of the variables shown in Fig. 4 and its removal is left for future work.

3. SIMULATED AND EXPERIMENTAL RESULTS

A board with these designs was fabricated (Kyocera) and characterised using a vector network analyser (VNA) and a digital communications analyser (DCA).

Several straight lines were fabricated for both the CBCPW and the SMCPW. The line characteristics were extracted using the Thru-only de-embedding procedure [17]. The results show a

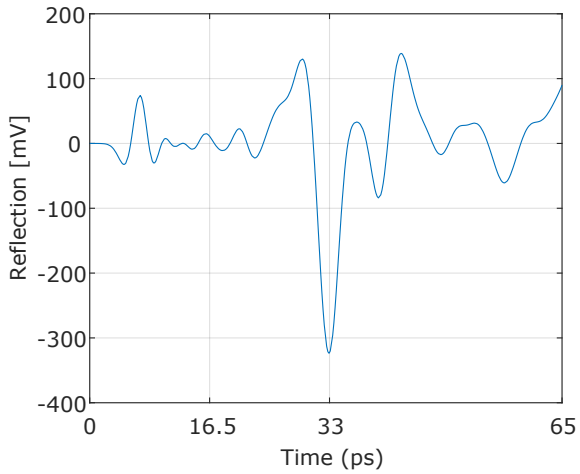

(a) Simulated reflection. The main reflection occurs at 33 ps

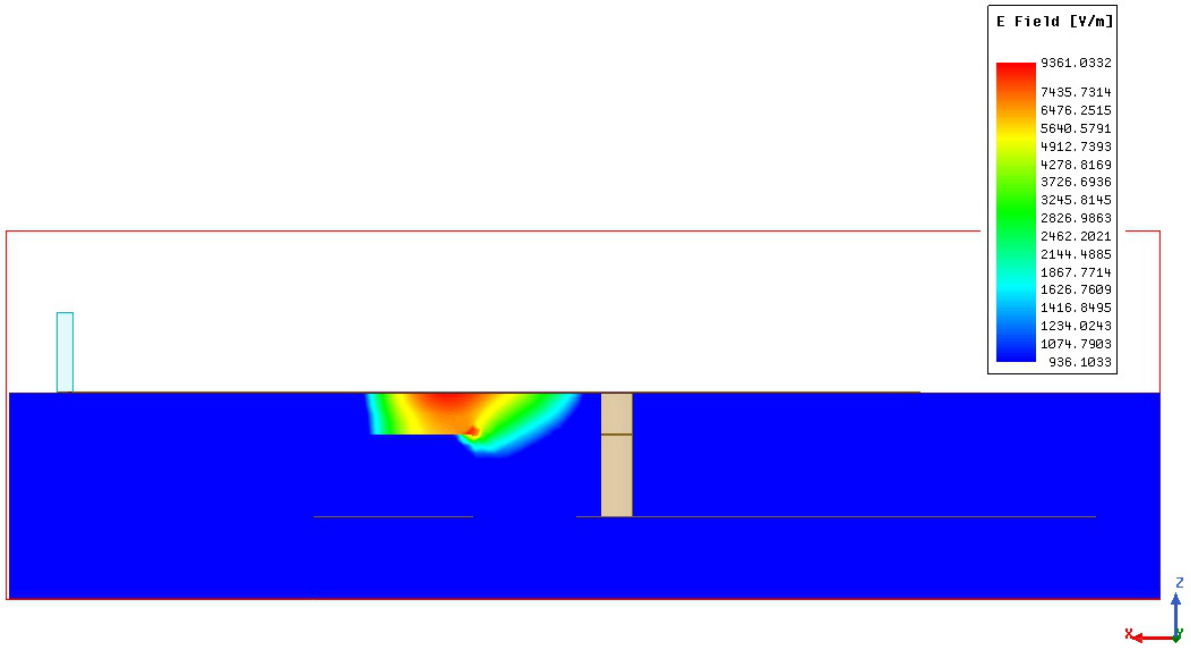

(b) The field cross-section at time 16.6 ps

Figure 7: The reflection of the initial version of the transition and the field at the time that creates the maximum reflection. Input voltage showed in Fig. 6a. The simulation can be used to locate the source of reflections.

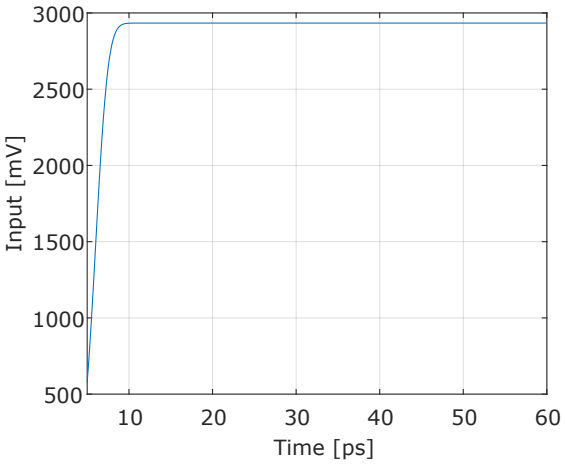

(a) Input voltage

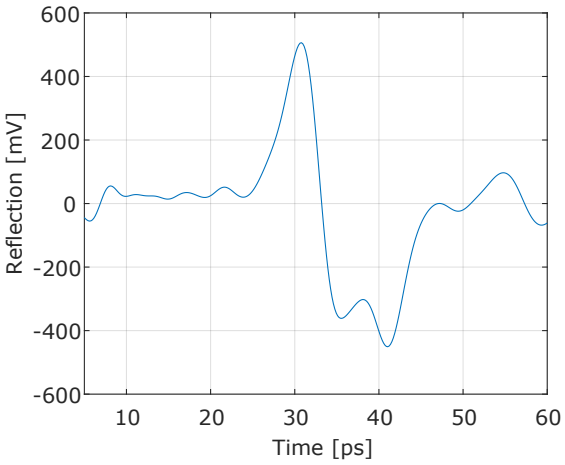

(b) Reflected voltage

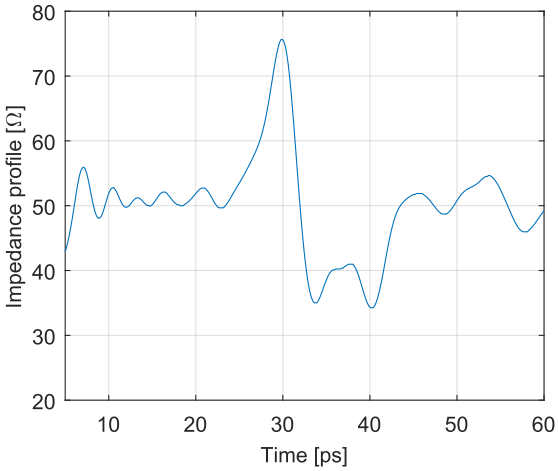

(c) Reconstructed impedance profile

Figure 8: The reconstructed impedance (c) from the integrated input voltage (b) and reflected voltage (a).

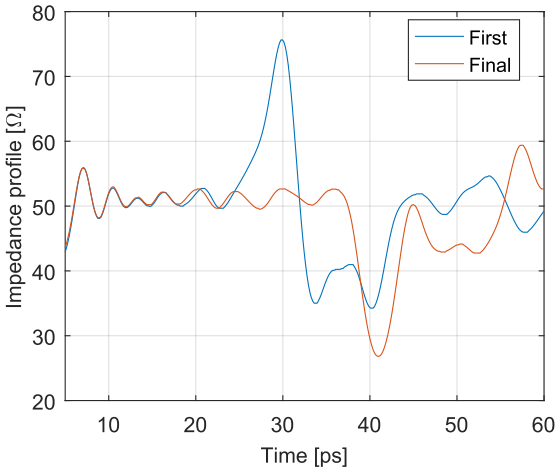

(a) Impedance reconstruction first version vs final version

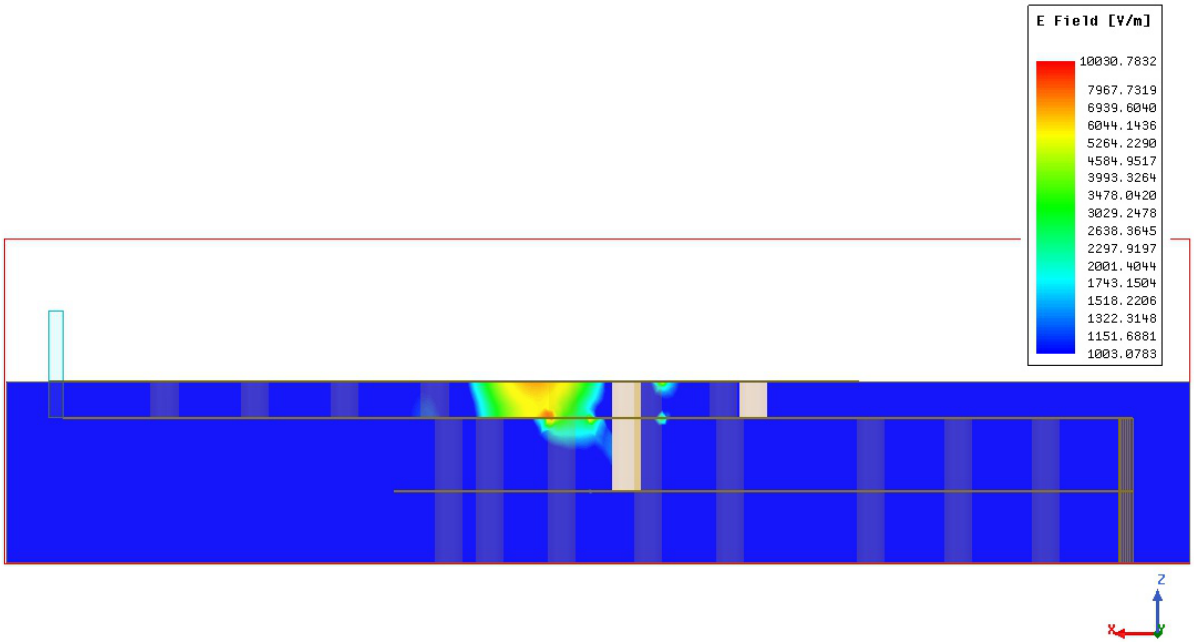

(b) The field cross-section at time 21 ps

Figure 9: A comparison of the reconstructed impedance profile for the first version and the final version. The final version presents a single low impedance section at 42 ps which relates to the events at time 21 ps.

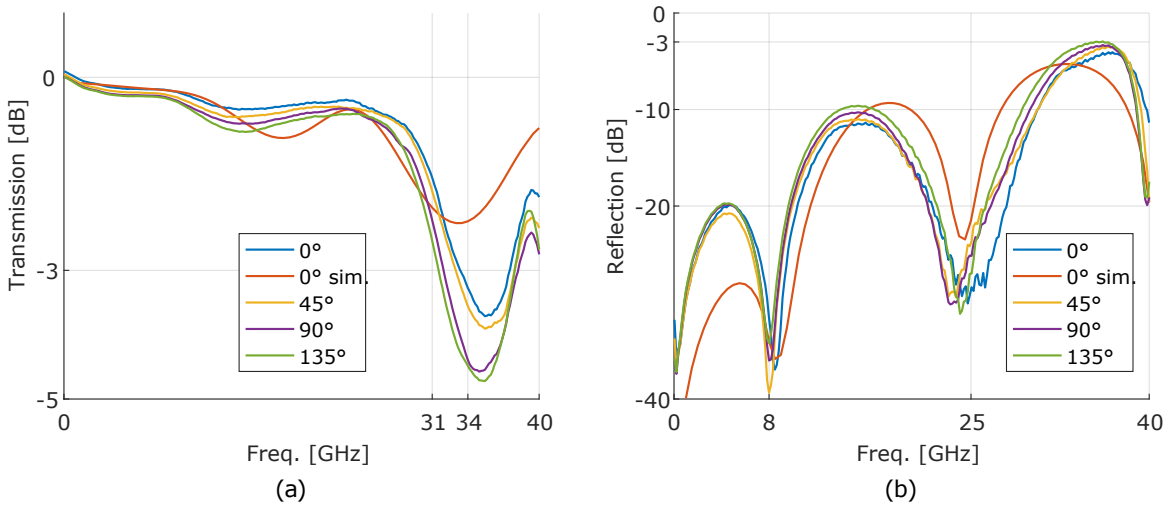

Figure 10: The transition showed good results in the VNA.

measured loss of $\approx 0.09\,\mathrm{dB\,mm^{-1}}$ at 40 GHz and 50 Ω characteristic impedance for both lines.

Several transitions with different angles were fabricated as shown in Fig. 2, the red line shows the buried path of the SMCPW. The transitions have two CBCPWs with a length of 1.7 mm and an SMCPW with a length of 3 mm. The transition was simulated using ANSYS HFSS. The full-wave simulation model uses frequency-independent material models based on the default values for air and gold and a single point measurement, provided by the supplier, at 2 GHz for AlN shown in Table 1. We used radiation boundary conditions and rectangular wave-ports to feed the model and a sweep from 1 GHz to 40 GHz in steps of 500 MHz.

The transition showed good results from the VNA measurement, and good agreement with the full-wave simulation, as shown in Fig. 10. Four structures, from the structures shown in Fig. 2, with angles of 0°, 45°, 90° and 135° between the CBCPW and the SMCPW were measured. The results of these measurements and the simulation of a straight transition (i.e. 0°) are shown in Fig. 10. The transmission (S_{21}) is shown in Fig. 10a and the reflection (S_{11}) in Fig. 10b. The transmission results show a 3 dB bandwidth between 31 GHz to 34 GHz. The bandwidth decreases with the rotation angle but the performance is still good for the larger angles. The simulation shows good agreement with the measurements in the transmission up to 30 GHz, but it fails to predict the minimum transmission around 34 GHz. The reflection is below −10 dB up to 25 GHz, and after that, it gets to a maximum of 3 dB around 34 GHz probably due to the frequency independent material models. The simulation also shows good agreement with the measurements in the reflection, correctly predicting the minimums at 8 GHz and 25 GHz.

The transition shows a good eye diagram in the (DCA), as shown in Fig. 11. A Pseudorandom Binary Sequence (PRBS) with a rate of $44\,\mathrm{Gbit\,s^{-1}}$ and a maximum length sequence of $2^7 - 1$ was launched into the transitions by using RF microwave probes. The measurement results account for the PRBS signal quality, the cables and the probes. To isolate the penalty due to the transitions, we first measured the through standard from a calibration substrate. This measurement represents the best performance that can be obtained with our test setup, and the results are shown in Fig. 11a. The measurement of the transition shown in Fig. 2 with a 90° turn is shown in Fig. 11b. The eye amplitude penalty, compared to the through standard, is only 24 mV and the eye width penalty only 0.14 ps thus good performance has been achieved at $44\,\mathrm{Gbit\,s^{-1}}$.

The channels showed crosstalk below −30 dB. An array of four phase-matched channels is shown in Fig. 12a. The array takes advantage of the transition's capacity to rotate and ease to bridge channels to avoid additional bends to equalize the phase length as in [18]. This demonstrates how contacts to closely spaced phase matched high speed modulators could be made in a packaged PIC. The S_{21} has been measured fixing one probe in channel 1 at the left of Fig. 12a and moving the second probe to each channel. The results (Fig. 12b) show that the crosstalk between adjacent channels (i.e. Channel 1 to Channel 2) is below −30 dB. This is evidence that the ground vias provide the necessary shielding against crosstalk.

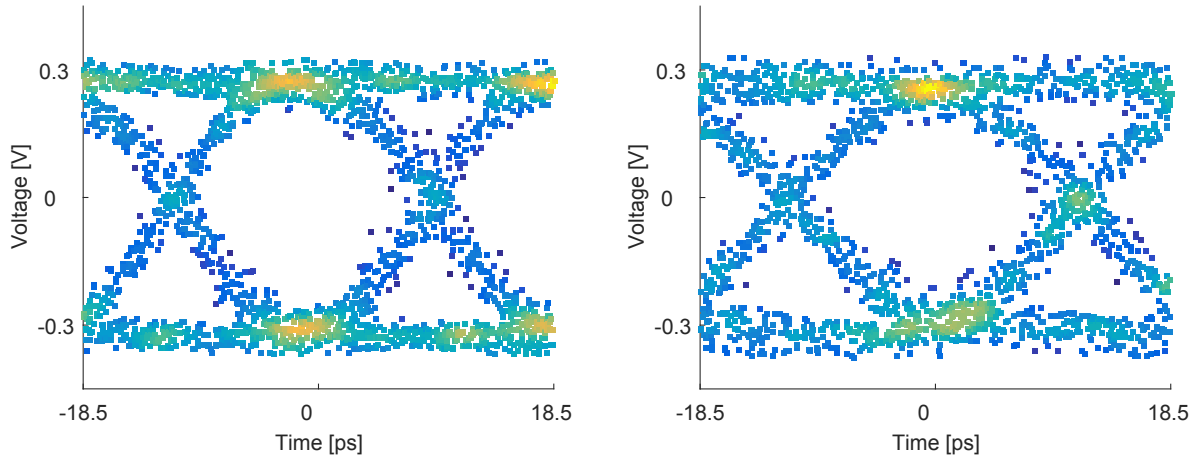

(a) Through from calibration substrate (b) Transition with 90° turn

Figure 11: The transition showed good results in the DCA.

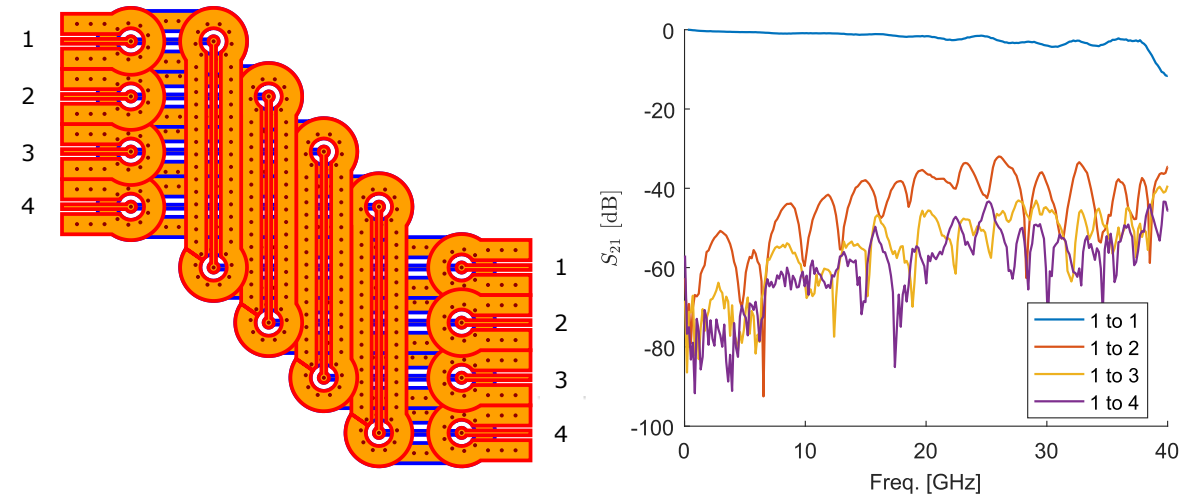

(a) Four phase-matched channels (b) Crosstalk results

Figure 12: Crosstalk below $-30\,\mathrm{dB}$ in adjacent channels in these four phase-matched channels array.

4. CONCLUSION

This article presented a high-speed multi-layer channel for co-fired AlN and its measured results. Two transmission lines were designed that showed a measured loss of $\approx 0.09\,\mathrm{dB\,mm^{-1}}$ at 40 GHz and 50 Ω characteristic impedance. The vertical transition allows for arbitrary planar rotations of the channel. The transition showed a measured 3 dB bandwidth between 31 GHz to 34 GHz and small penalties in the eye diagram with a $44\,\mathrm{Gbit\,s^{-1}}$ signal. The full-wave simulations agree with the measurements. The transition in co-fired AlN showed similar microwave performance than a similar version in Low-Temperature Co-fired Ceramic (LTCC) presented in [6]. Adjacent channels showed crosstalk below −30 dB. The channels are simple, fulfil the standard fabrication rules and use only three substrate layers. These results show the feasibility of using co-fired AlN as a packaging material for high-speed photonic devices where thermal management is needed.

In future work, we can improve the matching of the simulation with the measurements by using a frequency dependent microwave material parameters by extracting the material microwave parameters from the measurements. Additional investigation is needed to improve the reflection after 25 GHz.

ACKNOWLEDGMENT

Supported by the Science Foundation Ireland (SFI) under grants SFI10/CE/I1853 (CTVR II) and SFI12/RC/2276 (IPIC). This project has received funding from the European Research Council (ERC) under the European Union's Horizon 2020 research and innovation programme (grant agreement numbers 780283-MORPHIC and 700930-PICTURE).

REFERENCES

1. Fred Kish, Radhakrishnan NagaraJan., David Welch, Peter Evans, Jon Rossi, Jacco Pleumeekers, Andrew Dentai, Masaki Kato, Scott Corzine, RanJan.i Muthiah, Mehrdad Ziari, Richard Schneider, Mike Reffle, Tim Butrie, Damien Lambert, Mark Missey, Vikrant Lal, Matt Fisher, Sanjeev Murthy, Randal Salvatore, Scott DeMar.s, Adam James, and Chuck Joyner. From Visible Light-Emitting Diodes to Large-Scale III-V Photonic Integrated Circuits. *Proc. IEEE*, 101(10):2255–2270, Oct. 2013. doi: 10.1109/JPROC.2013.2275018.
2. R. Tummala. SOP: What Is It and Why? A New Microsystem-Integration Technology Paradigm-Moore's Law for System Integration of Miniaturized Convergent Systems of the Next Decade. *IEEE Trans. Adv. Packag.*, 27(2):241–249, May. 2004. doi: 10.1109/TADVP.2004.830354.
3. Ryan Enright, Shenghui Lei, Kevin Nolan, Ian Mathews, Alexandre Shen, Guillaume Levaufre, Ronan Friz-zell, Guang-Hua Duan, and Domhnaill Hernon. A Vision for Thermally Integrated Photonics Systems. *Bell Labs Tech. J.*, 19:31–45, 2014.
4. Eyad Arabi and Atif Shamim. Three-dimensional RF SoP technologies: LTCC versus LCP. *Microw. Opt. Technol. Lett.*, 57(2):434–441, Feb. 2015. doi: 10.1002/mop.28875.
5. F. Bechtold. A comprehensive overview on today's ceramic substrate technologies. *2009 Eur. Microelectron. Packag. Conf.*, 2009.
6. Moises A. Jezzini, P. J. Marraccini, and F. H. Peters. Design of a high-speed vertical transition in LTCC for interposers suitable for packaging photonic integrated circuits. In Laurent Vivien, Lorenzo Pavesi, and Stefano Pelli, editors, *SPIE Photonics Eur.*, page 98911R. International Society for Optics and Photonics, May. 2016. doi: 10.1117/12.2227628.
7. R. Sturdivant, Chung Ly, J. Benson, and M. Hauhe. Design and performance of a high density 3D microwave module. In *1997 IEEE MTT-S Int. Microw. Symp. Dig.*, volume 2, pages 501–504. IEEE, 1994. doi: 10.1109/MWSYM.1997.602841.
8. M Mantysalo and EO Ristolainen. Modeling and Analyzing Vertical Interconnections. *IEEE Trans. Adv. Packag.*, 29(2):335–342, May. 2006. doi: 10.1109/TADVP.2006.873137.
9. T. K. Johansen, C. Jiang, D. Hadziabdic, and V. Krozer. EM simulation accuracy enhancement for broadband modeling of on-wafer passive components. In *Proc. 37th Eur. Microw. Conf. EUMC*, pages 1245–1248. IEEE, 2007. doi: 10.1109/EUMC.2007.4405426.
10. Chenhui Jiang, Viktor Krozer, Tom K. Johansen, Heinz-Gunter Bach, Giorgis G. Mekonnen, and Lei Yan. Behavioral electromagnetic models of high-speed p-i-n photodiodes. *Microw. Opt. Technol. Lett.*, 53(11):2530–2533, Nov. 2011. doi: 10.1002/mop.26327.

11. F J Schmückle, R Doerner, G N Phung, W Heinrich, D Williams, and U Arz. Radiation , Multimode Propagation , and Substrate Modes in W-Band CPW Calibrations. In *Microw. Conf. (EuMC), 2011 41st Eur.*, pages 297–300, Manchester, 2011. IEEE.
12. Chenhui Jiang. *Microwave and Millimeter-Wave Integrated Circuit Systems in Packaging.* PhD thesis, Technical University of DenMar.k, 2010.
13. Muhammad Usman Sadiq. *Design and characterization of InP based Mach-Zehnder modulators at 2μm wavelength.* Doctoral thesis, University College Cork, 2016.
14. Uwe Arz, Martina Rohland, Karsten Kuhlmann, and Stephanus Buttgenbach. Wideband electromagnetic modeling of coplanar waveguides fabricated in membrane technology. In *2011 IEEE 15th Work. Signal Propag. Interconnects*, pages 129–130. IEEE, May. 2011. doi: 10.1109/SPI.2011.5898856.
15. Jacek Izydorczyk. Comments on "Time-domain reflectometry using arbitrary incident waveforms". *IEEE Trans. Microw. Theory Tech.*, 51(4):1296–1298, Apr. 2003. doi: 10.1109/TMTT.2003.809636.
16. J Izydorczyk. Microwave time domain reflectometry. *Electron. Lett.*, 41(15):848, 2005. doi: 10.1049/el:20051696.
17. A.M. Mangan, S.P. Voinigescu, Ming-Ta Yang, and Mihai Tazlauanu. De-embedding transmission line measurements for accurate modeling of IC designs. *IEEE Trans. Electron Devices*, 53(2):235–241, Feb. 2006. doi: 10.1109/TED.2005.861726.
18. Yanbo Li, Hua Yang, M. Jezzini, P.E. Morrissey, B. Corbett, N. Kelly, M.U. Sadiq, F.H. Peters, M. Crowley, P.J. Marraccini, and Lei Gao. Phase matched transmission line design for high-speed optical modulators. In *25th IET Irish Signals Syst. Conf. 2014 2014 China-irel. Int. Conf. Inf. Communities Technol. (ISSC 2014/CIICT 2014)*, pages 135–140. IET, Institution of Engineering and Technology, 2014.